ADVANCED INTELLIGENT SYSTEMS
Open Access
www.advintellsyst.com

Thermally Responsive Architected Actuators with Programmable Shape Morphing and Tunable Stiffness

*Yu Chen, Xudong Yang, Tianyu Chen, Junwei Li, and Yifan Wang**

Biological organisms excel in dynamically reshaping their bodies to navigate and manipulate ever-changing environments, and some can even tune their mechanical properties for enhanced adaptability. Many existing shape-morphing robots rely on the inherent softness of materials or structures, which sacrifices load-bearing capacity. Despite efforts to achieve both morphing and stiffness tuning in one system, these strategies often rely on separate mechanisms, such as heating liquid metal components to reduce rigidity before employing other mechanisms to change the shape, leading to bulky and complex systems that limit practicality and scalability. Here, a tunable-stiffness architected morphing structure (TSAMS) is introduced, which unifies shape morphing and tunable stiffness in a single, compact platform. By combining 3D-printed tessellated particles with shape memory alloy springs, TSAMS transitions smoothly from soft to rigid states, exhibiting a ≈308 times increase in bending stiffness while concurrently executing intricate shape transformations through electrothermal actuation. This design is demonstrated with the following robotic applications, including rolling robots that can explore diverse terrains by climbing slopes, avoiding obstacles, and carrying loads; compact manipulators that lift objects nearly 50 times heavier than themselves; and snake-inspired robots performing undulation and sidewinding gaits. These results highlight TSAMS's potential to advance next-generation soft robots and bioinspired systems that demand both dynamic shape reconfiguration and robust structural performance in diverse operating conditions.

1. Introduction

The ability to transform shape and adjust mechanical properties, ranging from subtle postural adjustments to dramatic life-stage changes, is a defining feature of natural organisms.[1,2] Across the animal[3] and plant[4] kingdoms, this remarkable capability manifests in diverse ways—armadillos curling into protective coils, octopuses contorting through tight confines, and Venus flytraps snapping shut around prey. These extraordinary adaptations, refined through countless generations of evolution,[5] involve not only shape transformation but also dynamic tuning of mechanical properties,[6,7] such as stiffness, to enhance functionality in ever-changing environments. Inspired by these natural strategies, researchers aim to develop artificial robotic systems capable of integrating shape-morphing capabilities with tunable mechanical properties.[8–12]

To achieve active shape morphing, various studies have utilized inherently soft materials, such as stimuli-responsive polymers[13,14] and liquid crystal elastomers.[15,16] While these methods allow for actuators with bending, folding, or twisting deformations, they impose significant constraints on load-bearing capability and structural stability.[17] Attempts to overcome this limitation involve combining separate systems for shape morphing and stiffness control, such as heating liquid metal components to reduce rigidity before activating pneumatic actuators to change shape.[18] However, these approaches are inherently complex, requiring multi-step processes, multiple power sources, and sequential operations without concurrent stiffness tuning and shape morphing. In stark contrast, natural organisms achieve a seamless balance between flexibility and stiffness,[19–21] dynamically adapting themselves as needed. For example, elephant trunks and octopus tentacles maintain compliance to navigate complex environments while dynamically stiffening to exert force for robust grasping or precise manipulation. This elegant integration of shape changes and stiffness tuning in biological systems highlights the limitations of current soft robotic systems and underscores the need for innovative approaches to achieve multifunctional, highly integrated morphing and stiffening capabilities.

In this work, we draw inspiration from the segmented biological systems—such as crayfish shells and snake spines

Y. Chen, X. Yang, T. Chen, J. Li, Y. Wang
School of Mechanical and Aerospace Engineering
Nanyang Technological University
Singapore 639798, Singapore
E-mail: yifan.wang@ntu.edu.sg

X. Yang
Agency for Science
Technology and Research (A*STAR)
Singapore Institute of Manufacturing Technology (SIMTech)
2 Fusionopolis Way, Singapore 138634, Singapore

The ORCID identification number(s) for the author(s) of this article can be found under https://doi.org/10.1002/aisy.202500123.

© 2025 The Author(s). Advanced Intelligent Systems published by Wiley-VCH GmbH. This is an open access article under the terms of the Creative Commons Attribution License, which permits use, distribution and reproduction in any medium, provided the original work is properly cited.

DOI: 10.1002/aisy.202500123

(**Figure 1**a)—where rigid units are interconnected to enable smooth morphing and stiffness tuning under muscular actuation for locomotion and protection. We introduce the tunable-stiffness architected morphing structure (TSAMS), which utilizes 3D-printed architected particles coupled with shape memory alloy (SMA) springs to achieve simultaneous shape morphing and stiffness tuning (≈308 times bending stiffness change) driven by thermal stimuli. We demonstrate the versatility of TSAMS through several robotic prototypes. First, we showcase an untethered rolling robot capable of obstacle avoidance, slope climbing, and carrying loads. Next, we present a 3-degree-of-freedom (3-DOF) manipulator, featuring a twisting base and a bending end effector capable of lifting objects ≈50 times its own weight. Additionally, a snake-like robot is developed to highlight how morphing pattern shifting enables both lateral undulation and sidewinding locomotion. By leveraging tessellated particles actuated through electrothermal actuators, this approach represents a significant advancement in the design of morphing robots, which combines ease of fabrication with dynamically tunable mechanical properties, offering a pathway toward more versatile, robust, and adaptive robotic systems in diverse environments.

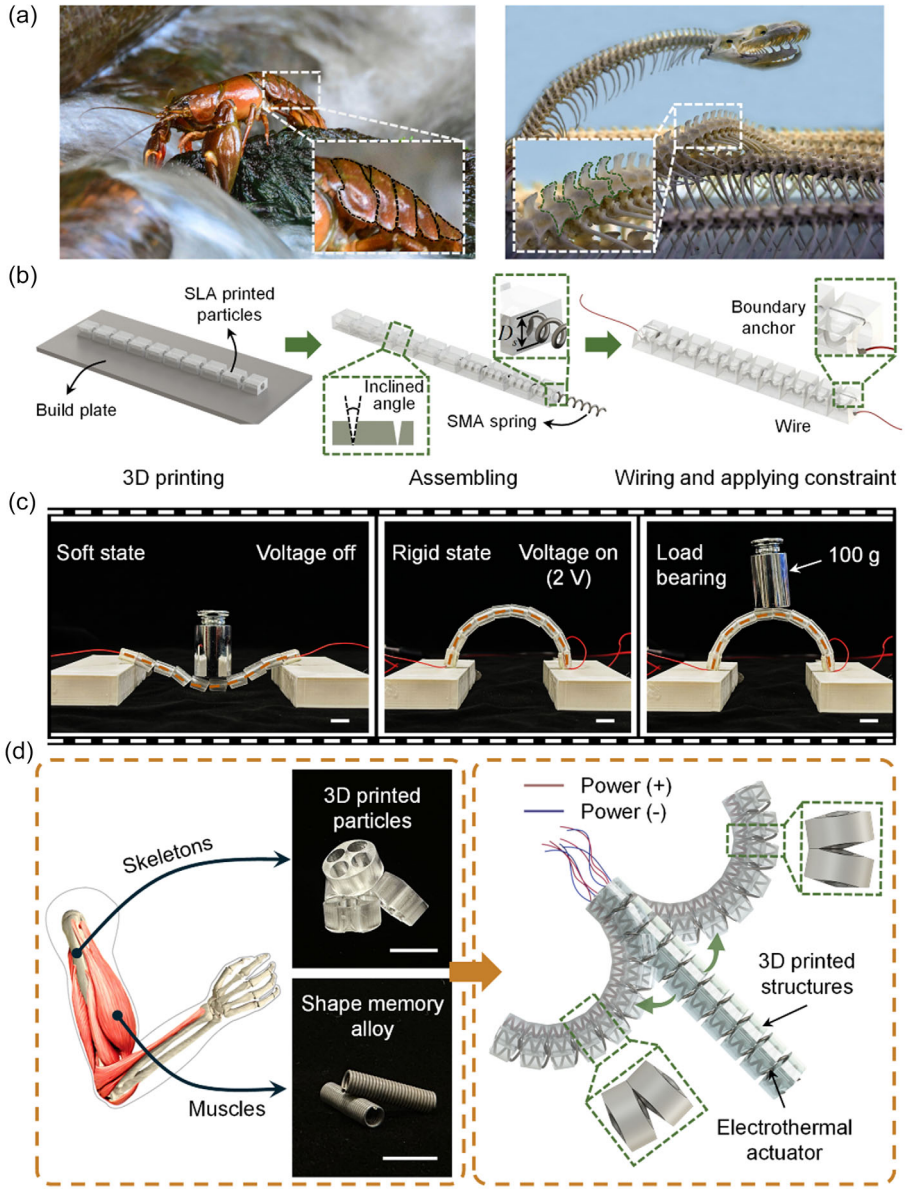


Figure 1. Bioinspiration, design, fabrication, and experimental demonstration of TSAMS. a) Bioinspiration from the tessellated architectures of crayfish shells, and snake spines with a designed morphing pattern. b) The design and fabrication process of TSAMS, including 3D printing of particles, assembling particles with electrothermal actuators (SMA springs), and wiring and applying boundary constraints. c) The experimental demonstration of the shape morphing and stiffness tuning capability of TSAMS. d) Potential application of TSAMS as a soft manipulator, utilizing 3D-printed particles as the "skeleton" and SMA springs as the "muscle". Scale bar, 1 cm.

© 2025 The Author(s). Advanced Intelligent Systems published by Wiley-VCH GmbH

2. Results and Discussion

2.1. Design Principles and Fabrication Process

The design of the TSAMS is primarily inspired by the segmentation architectures observed in nature. From the protective organisms of crayfish to the spinal skeletons of snakes (Figure 1a), these natural structures consist of rigid units interconnected by soft materials such as ligaments,[22] collagen fibers,[23] and chitin fibrils.[24] This combination allows for smooth shape morphing under muscular actuation. Translating these principles into robotics, TSAMS integrates architected particles with SMA springs to create a versatile and programmable morphing framework.

We select trapezoidal particles as the basic structural elements, featuring predetermined inclined angles between adjacent particles.[25,26] By arranging these particles in a pre-defined sequence, a curved structure can be achieved when the particles are compressed together. The particles with designed geometries are fabricated using stereolithography (SLA) 3D printing, ensuring high precision and structural integrity. Additionally, hollow channels are designed in these particles to allow for the insertion of the SMA actuators. After printing, SMA springs are inserted to serve as soft connectors as well as thermal actuators. Thin electric wires are then soldered to the tips of the SMA springs for electrothermal actuation, and boundary constraints are applied between the SMA springs and the end particles using steel fibers and UV light-cured glue, as shown in Figure 1b (see Experimental Section, Figure S1, Supporting Information). The mechanical properties of the SLA-printed particles and the electro-thermo-mechanical performance of the SMA springs are detailed in Figure S2 and Table S1, Supporting Information, respectively.

The concurrent shape morphing and stiffness tuning capabilities of TSAMS are experimentally demonstrated in Figure 1c. In its relaxed state with no voltage applied, TSAMS remains soft, allowing free bending as the particles easily separate under external loads. Upon the application of voltage, the SMA springs undergo electrothermal heating and contraction, driving the particles to assemble into a target configuration (e.g., a 180° arc) under the imposed boundary constraints. Once fully assembled, TSAMS transitions to a rigid state, demonstrating its ability to support a load of 100 g, which is over 15.8 times its own weight (Figure S3, Supporting Information).

In the design of TSAMS, the 3D-printed particles serve as the structural skeleton, while the SMA springs function as muscular actuators. By assembling the TSAMS units in series or in parallel, we can construct soft manipulators with multiple degrees of freedom, capable of bearing loads several times their own weight (Figure 1d). This modular approach enables the development of complex, multifunctional robotic systems that combine the advantages of flexible morphing and tunable mechanical properties, paving the way for versatile applications in diverse environments.

2.2. Characterization of Shape Morphing and Stiffness Tuning Abilities

TSAMS is designed to achieve reconfigurable shape transformations through the actuation of the electrothermal actuator and the assembly of tessellated architected particles. As illustrated in **Figure 2**a, the morphing process begins with the assembly of trapezoidal particles to form an arc-shaped TSAMS. In the absence of applied voltage, the SMA springs remain in a plastically elongated state maintaining gaps between adjacent particles, which make the entire TSAMS structure highly compliant and easy to bend under external loads. Upon applying voltage, the SMA springs undergo electrothermal heating and contract, compressing the adjacent particles into close contact while morphing the entire structure into the target shape. Experimental validation demonstrates that TSAMS can reliably achieve various one-dimensional shapes, such as wave and hook geometries (Figure 2b). The actuation is achieved using a voltage of 2 V. Furthermore, the TSAMS exhibits modularity and reconfigurability by morphing into two or more distinct shapes when additional layers are attached (Figure 2c, Figure S4, Supporting Information). In the two-layer structure, the contraction force generated by the SMA spring on the actuated side is sufficient to overcome the bending stiffness of the opposing side, enabling the structure to seamlessly transition into the selected shape.

In addition to shape morphing, TSAMS offers remarkable capabilities in stiffness tuning. Unlike conventional stiffness-changing robotic structures that rely on light,[27] fluidic pressure,[28] or magnetic fields,[29] TSAMS employs a more streamlined and integrated approach. By controlling the actuating voltage applied to the SMA springs, the system regulates the contact forces between tessellated particles,[25,26,30,31] thereby modulating the overall bending stiffness of the structure.

To quantitatively assess the stiffness tunability of TSAMS, we first examine a simplified one-dimensional configuration: a beam composed of nine cubic particles with a total length of 9 cm. Figure 2d illustrates the experimental setup for cantilever bending tests, which were conducted to evaluate the mechanical properties of TSAMS under different actuating voltages (see Experimental Section for detailed setup). The force–displacement curves in Figure 2e demonstrate that as the actuating voltage increases from 0 to 3.2 V, the bending force at a displacement of 8 mm rises from ≈0.050 N to ≈0.62 N. This elastoplastic behavior is attributed to the interaction between the SMA springs and the tessellated particles during deformation. Specifically, the deformation process can be divided into two distinct stages:[31] i) The pre-separation stage, where the contraction force generated in SMA springs is sufficient to drive adjacent particles into tight contact, and the segmented beam can be treated as a continuous beam. ii) The separation stage, during which the external bending force continuously increases, causes the particles to gradually separate, resulting in a plateau region in the force–displacement curves. Importantly, the force–displacement curves rise significantly with the actuating voltage increasing from 0 to 3.2 V. This is attributed to the stronger boundary confinement on the particles, resulting in a higher effective elastic modulus in the first stage.[25]

To investigate the impact of particle geometry on TSAMS' mechanical properties, we conducted the same cantilever bending tests on TSAMS structures with varying inclined angles (i.e., $\alpha = 50°$, 60°, 70°, 80°, and 90°). To ensure consistency, all samples featured a square medial section with $L = 10$ mm and a height of $h = 10$ mm (Figure S5, Supporting Information). We obtain the bending stiffness from the slope of the initial elastic regime (displacement within ≈1 mm) in the force–displacement curves

© 2025 The Author(s). Advanced Intelligent Systems published by Wiley-VCH GmbH

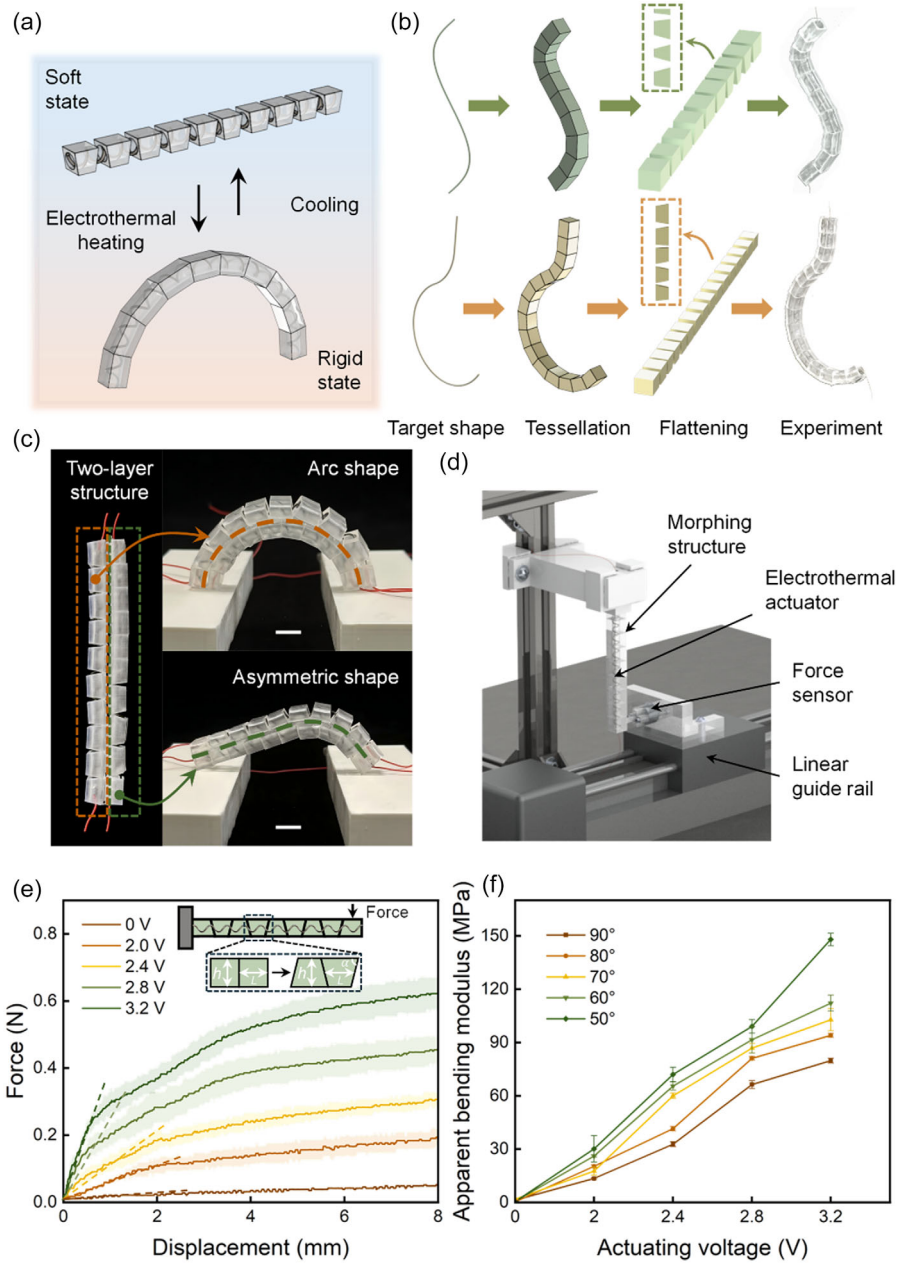


Figure 2. Characterization of TSAMS's shape morphing and stiffness-tuning capabilities. a) Morphing and recovering cycle of an arc-shaped TSAMS composed of trapezoidal particles with square cross-sections. b) Inverse design process for achieving different one-dimensional shapes (wave and hook), including target shape design, tessellation, flattening, and experimental validation. c) A single TSAMS morphing into two distinct shapes by attaching two layers together. Scale bar, 1 cm. d) Experimental setup for cantilever bending tests to evaluate the mechanical properties of TSAMS. e) Force–displacement curves from cantilever bending tests of TSAMS with 90° inclined angles at various actuating voltages. Colored lines represent average values, and shaded areas denote standard deviations from three independent tests. f) Comparison of the apparent bending modulus of TSAMS with different inclined angles under actuating voltages ranging from 0 to 3.2 V. Colored lines represent average values, and error bars denote standard deviations from three independent tests.

and calculated the apparent bending modulus for each sample under different actuating voltages (Figure 2f, see Experimental Section for the calculation of the apparent bending modulus). It is observed that as the inclined angle decreases from 90° to 50°, the apparent bending modulus under a 3.2 V actuating voltage increases from ≈79.8 MPa to ≈148.0 MPa, indicating a significant increase in the stiffness of TSAMS. The relationship between inclined angle and stiffness modulation highlights the influence of geometric design on mechanical performance, where smaller angles facilitate more efficient stiffness tuning by requiring larger opening angles under loading, resulting in greater force responses and higher stiffness.

© 2025 The Author(s). Advanced Intelligent Systems published by Wiley-VCH GmbH

We also measure the apparent bending modulus of TSAMS without actuating voltage applied, where the SMA springs are soft and allow for plastic deformation. The results indicate that the stiffness variation ratio can reach ≈63 ($\alpha = 90°$)-308 ($\alpha = 50°$) times between the stiff and soft states (Figure S5, Table S2, Supporting Information). This ability to dynamically modulate stiffness while maintaining shape morphing provides TSAMS with enhanced adaptability and robustness, making it well-suited for applications requiring variable load-bearing capacities and versatile morphing capabilities.

2.3. Untethered Thermal-Driven Self-Rolling Robots from TSAMS

To demonstrate the functionality of TSAMS in adaptive robotics, we redesign the particle geometry and create a circular assembly of four units to develop thermally driven self-rolling robots. The design and fabrication process of the rolling robot is illustrated in **Figure 3**a. A 180° arc is selected as the target shape, which is tessellated into 10 identical particles, each with a central angle $\varphi = 18°$ (inclined angle $\alpha = 81°$). The particle cross-section is designed as a quadrant, allowing the circular assembly of four units to form a complete circle in the cross-section. After assembling and flattening the design, the particles are fabricated using an SLA printer, and SMA springs are integrated for actuation (see Experimental Section for detailed fabrication process).

Two distinct robot designs are developed, differentiated by their cross-sections: concentric and eccentric types (Figure 3b). The concentric design features symmetrically arranged thermal actuators, requiring an initial C-bend to ensure consistent rolling in a single direction. In self-rolling robots, body curvature significantly influences the rolling direction by modulating the rolling torque.[32,33] When the pre-bent robot is placed on a heating plate, the SMA spring closest to the plate (on the underside of the robot) activates first, causing the robot to bend upward slightly. The torque generated by the axial force in activating SMA spring, and the imbalance between ground interaction and gravity drives the robot to fall toward the outer side of the C-bend curvature (see Figure S6, Supporting Information for more details). This movement positions the adjacent SMA spring as the closest to the heating plate, which is then activated, as shown in Figure 3c. This sequential contraction and relaxation of SMA springs continuously alters the opening of the C-bend curvature, driving the

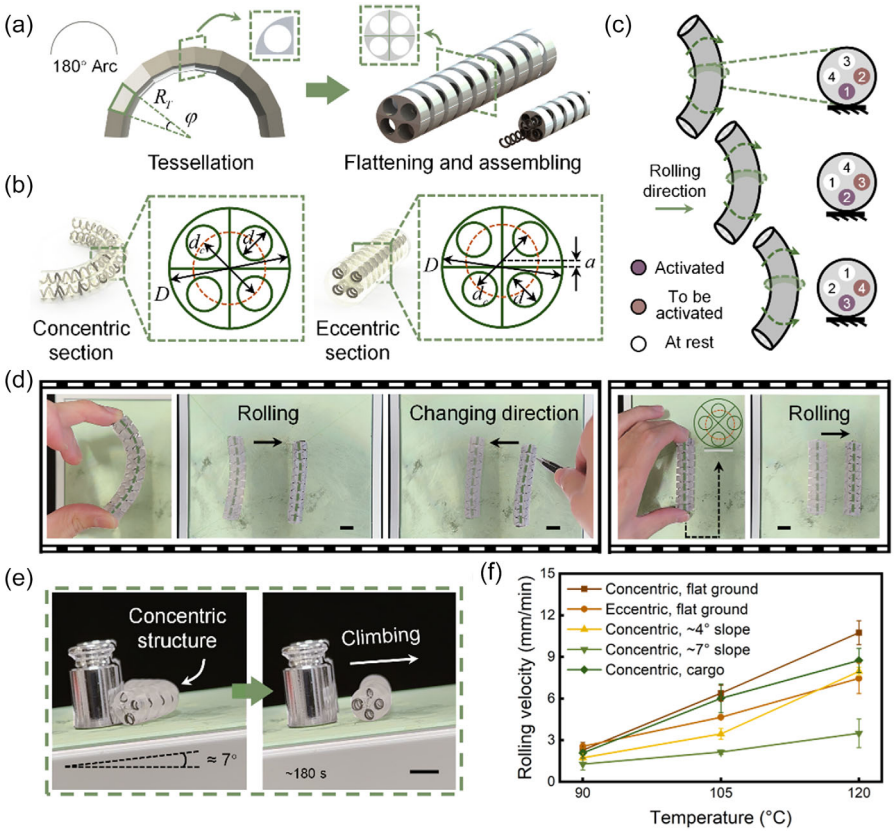


Figure 3. Untethered self-rolling robots constructed from circular-assembled TSAMS on a heating plate (90 °C). a) Design and fabrication process of the self-rolling robot. b) Two distinct robot designs featuring concentric and eccentric particle cross-sections. c) Demonstration of continuous rolling of the bent concentric robot achieved by sequential actuation. d) In the concentric design, initial bending forms body curvature, determining the robot's rolling direction. In contrast, the eccentric design predefines the rolling direction through asymmetrical gravity distribution and heat conduction. e) The concentric robot climbs slope up to 7 degrees. f) Speed measurements of the robots under various locomotion scenarios on the heating plate at different temperatures (90, 105, and 120 °C), including flat ground rolling, slope climbing, and cargo transportation. Colored lines represent average values, and error bars denote standard deviations from three independent tests. Scale bar, 1 cm.

© 2025 The Author(s). Advanced Intelligent Systems published by Wiley-VCH GmbH

robot to roll toward the outer side of the C-bend (Movie S1, Supporting Information). The robot harnesses thermal energy from the hotplate substrate to power itself, enabling continuous rolling locomotion. The eccentric design, in contrast, employs an asymmetrical arrangement of SMA springs to introduce a directional bias in rolling behavior. This eliminates the need for an initial C-bend, as the structural asymmetry inherently biases the rolling direction. When placed on a heating plate, the eccentric robot rolls consistently in a predetermined direction without relying on body curvature, simplifying operation and enhancing autonomy (Figure 3d). This advancement makes the eccentric design more practical for applications requiring minimal setup and reliable directional control. Figure 3e demonstrates that the concentric-designed robot can continuously roll up a 7-degree slope. Additional locomotion scenarios, including curvature reversal upon obstacle contact, slope climbing, and cargo transportation, are shown in Figure S7, Supporting Information, to further illustrate the robot's environmental adaptability and functional potential.

We summarize the rolling velocities of the robot under various scenarios on the heating plate at different temperatures (90, 105, and 120 °C) in Figure 3f, encompassing flat ground rolling, slope climbing, and cargo transportation. The results demonstrate a clear trend: rolling velocity increases with the temperature of the heating plate. Notably, on the 120 °C heating plate, the flat ground rolling velocity is approximately three times higher than that observed at 90 °C. Furthermore, as shown in Movie S5, Supporting Information, the rolling velocity increases even further when the temperature is raised to 150 °C. Additional tests under high-humidity conditions (≈80%) were conducted to evaluate environmental robustness, revealing minimal differences in rolling speed compared to standard conditions (55% humidity) at both 90 °C and 120 °C heating temperatures, as shown in Figure S8 and Movie S5, Supporting Information.

Compared to the existing thermal-driven self-rolling robots, our design offers several distinct advantages. Unlike many soft rolling robots, such as liquid crystal elastomer (LCE) rolling robots, which require a time-intensive synthesis process (over 12 h),[15,32] the robots leverage a straightforward yet effective mechanical design and are fabricated from common, affordable materials. This approach reduces both fabrication complexity and cost. Additionally, the proposed robots function efficiently on surfaces with temperatures above the austenite start temperature of the SMA springs (≈50 °C),[34] which is substantially lower than the working temperature required by LCE rolling robots (e.g., >160 °C,[15] ≈100 °C[35]). These features collectively position the proposed rolling robots as a practical, efficient, and cost-effective solution for a wide range of applications.

2.4. A 3-DoF Manipulator from TSAMS

Various studies have highlighted that structures with variable stiffness are promising candidates for the development of soft manipulators.[36,37] In this application, we integrate shape-morphing and variable-stiffness functionalities into a 3-DoF soft manipulator utilizing TSAMS. As illustrated in **Figure 4**, the manipulator comprises a bending end effector and a twisting base, both assembled using 4 TSAMS units.

For the bending end effector, we employ a design similar to that of the thermally driven self-rolling robot. A 180-degree arc is tessellated into 10 identical particles, each with a quadrant cross-section and an intersection angle $\gamma = 18°$ between adjacent particles. Four quadrant units are assembled to form a complete circle, with four SMA springs inserted and wired for actuation. This configuration enables the end effector to bend in four directions by selectively actuating each SMA spring (Figure 4a). Figure 4b illustrates the inverse design process for the two-directional twisting base, where the bending motion of individual TSAMS units is transformed into twisting motion by leveraging the morphing capabilities of 4 radially arranged TSAMS units. The top and bottom plates of the twisting base are square, with a side length of L. The key parameters governing the design are the twist angle θ and the rotation radius R. Once R and θ are determined, the displacement d can be calculated accordingly. To achieve simpler and more precise morphing, a centrosymmetric design is adopted for the target shape of each TSAMS unit, where $d_f = \frac{1}{2}d$. The radius angle β, radius r, and length l are optimized to ensure a smooth and stable morphing process (see Experimental Section for more details).

To validate the effectiveness of our design, we conduct experiments to demonstrate the morphing capability and load-bearing capacity of the bending end effector and the twisting base. Figure 4c shows the morphing process of the end effector in a single direction, achieved by actuating one SMA spring. To evaluate the load-bearing capacity and the relationship between loading and shape morphing, we compare the morphed shapes of the end effector under varying loads ranging from 0 to 250 g, as depicted in Figure 4d (see Experimental Section, Figure S9 and S10, Supporting Information for more details). The stiffness tuning ability of TSAMS allows the end effector, despite its lightweight design of ≈6 g, to support a maximum load of 250 g (≈40 times its weight), highlighting its remarkable load-bearing capacity (Movie S6, Figure S11, Supporting Information). The curves indicate that under a load of 50 g, the morphed curvature closely resembles that observed with no load, highlighting the robustness and reliability of the proposed end effector. In addition, a drop test was conducted to evaluate the manipulator's response under dynamic loading conditions, with a 50 g weight dropped from a height of 5 cm, resulting in an impact velocity of $\approx 0.99\ \mathrm{m\,s^{-1}}$, further demonstrating its resilience (see Experimental Section, Figure S12, Supporting Information for details). We further explore the complex morphing behavior of the end effector by simultaneously actuating two SMA springs with different control patterns, as shown in Figure 4e and Movie S7, Supporting Information. By adjusting the actuating voltage of each SMA spring, the end effector is capable of not only achieving four-directional bending but also moving along a circular trajectory and stopping at any position on the trajectory (see Experimental Section for further details). This level of controlled morphing behavior makes the proposed end effector an excellent candidate for a wide range of manipulation tasks.

Similarly, the target morphing posture alongside its experimental demonstration of the twisting base is shown in Figure 4f. The four TSAMS units are divided into two pairs with opposing morphing directions, each arranged diagonally (indicated by the green and orange dashed lines in Figure 4f).

© 2025 The Author(s). Advanced Intelligent Systems published by Wiley-VCH GmbH

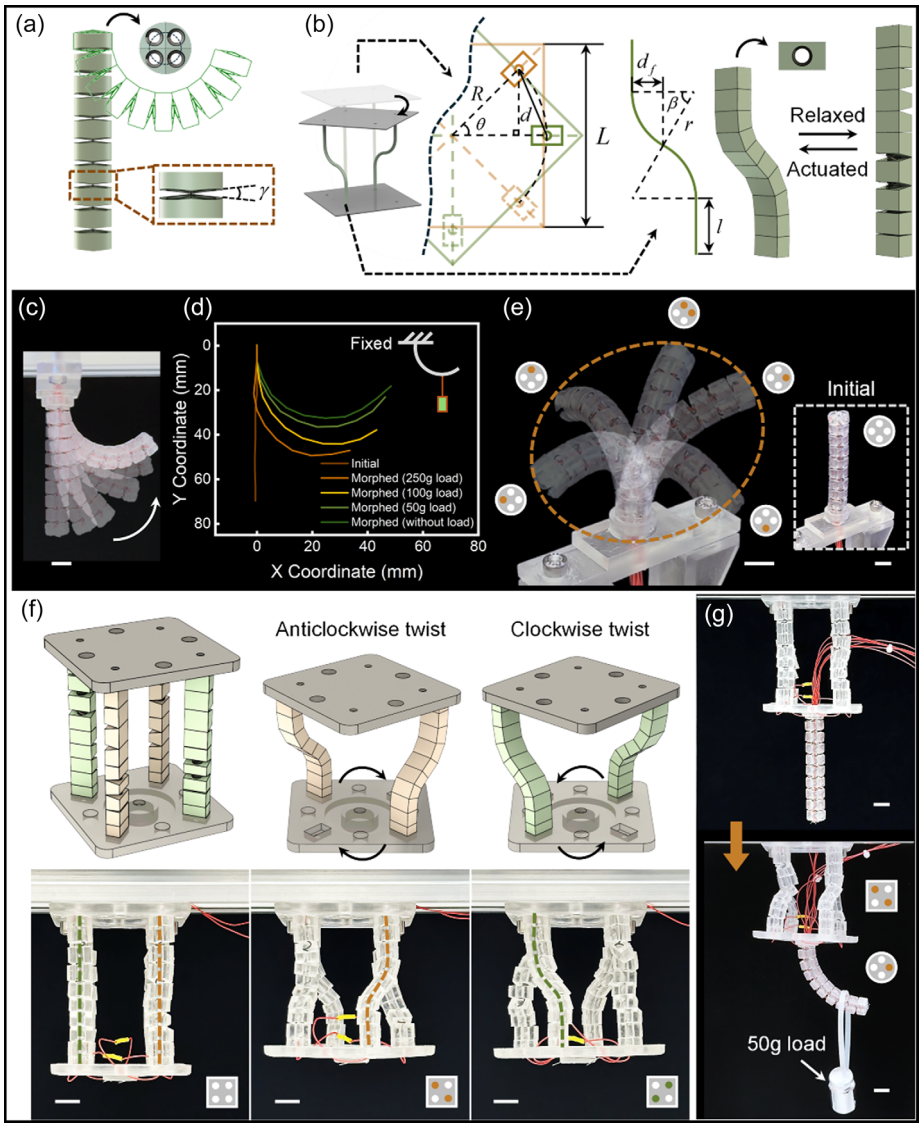


Figure 4. The 3-DoF soft manipulator consisted of a bending end effector and a twisting base. a) Inverse design of circular-assembled TSAMS units enabling multi-directional bending of the end effector. b) Inverse design of radially arranged TSAMS units enabling two-directional twisting of the robotic base. c) Experimental demonstration of the morphing process of the end effector actuated by a single electrothermal actuator. d) Comparison of the morphed shapes of the end effector under different loads, ranging from 0 to 250 g. e) Demonstration of the end effector morphing into different directions and moving along a circular trajectory under various control patterns. f) Design and experimental demonstration of the twisting base under various control patterns. g) Integration of the twisting base and the end effector to develop a 3-DoF soft manipulator. Scale bar, 1 cm.

The SMA springs within each pair are series-connected, enabling simultaneous actuation. By switching the actuation control pattern between the two pairs, the base can achieve both clockwise and counterclockwise twisting motions.

We then integrate the twisting base and the bending end effector to construct the 3-DoF soft manipulator, as illustrated in Figure 4g and Movie S8, Supporting Information. The two components can be independently controlled, enabling highly customizable manipulation. The stiffness-tuning capability of the manipulator enables it to support loads of up to 250 g despite weighing only ≈51 g (twisting base ≈45 g, end effector ≈6 g, Figure S11, Supporting Information). This exceptional load-bearing performance makes it well-suited for applications in weight-sensitive or space-constrained environments. Moreover, by adjusting the actuating voltage, the manipulator can maintain intermediate postures between its initial and fully morphed states, allowing precise control while manipulating objects (Movie S8). The proposed manipulator offers several advantages, including easy fabrication, efficient load-bearing performance relative to its weight, and versatile posture control, making it an effective solution for complex manipulation tasks. These features demonstrate the practicality and robustness of the design, positioning it as a promising tool for applications requiring adaptable and lightweight robotic systems.

© 2025 The Author(s). Advanced Intelligent Systems published by Wiley-VCH GmbH

2.5. A Crawling Robot from TSAMS

Snakes are widely recognized as exemplary models for the development of bioinspired robots due to their remarkable locomotive capabilities.[38–41] Among their diverse range of movement patterns, sidewinding, and lateral undulation are the most prevalent gaits, both featuring wave-like motion profiles.[42,43] In this work, we construct a snake-inspired robot by linking three two-layer TSAMS segments to achieve both lateral undulation and sidewinding via a simple switch of the control pattern. As illustrated in **Figure 5**a, each individual layer within a segment is designed to morph into a 180-degree arc, similar to rolling robots and soft manipulators. With two layers attached, each segment can achieve bidirectional morphing by selectively actuating one layer at a time. This arc is tessellated into 10 rectangular particles, which are 3D printed and integrated with the actuators.

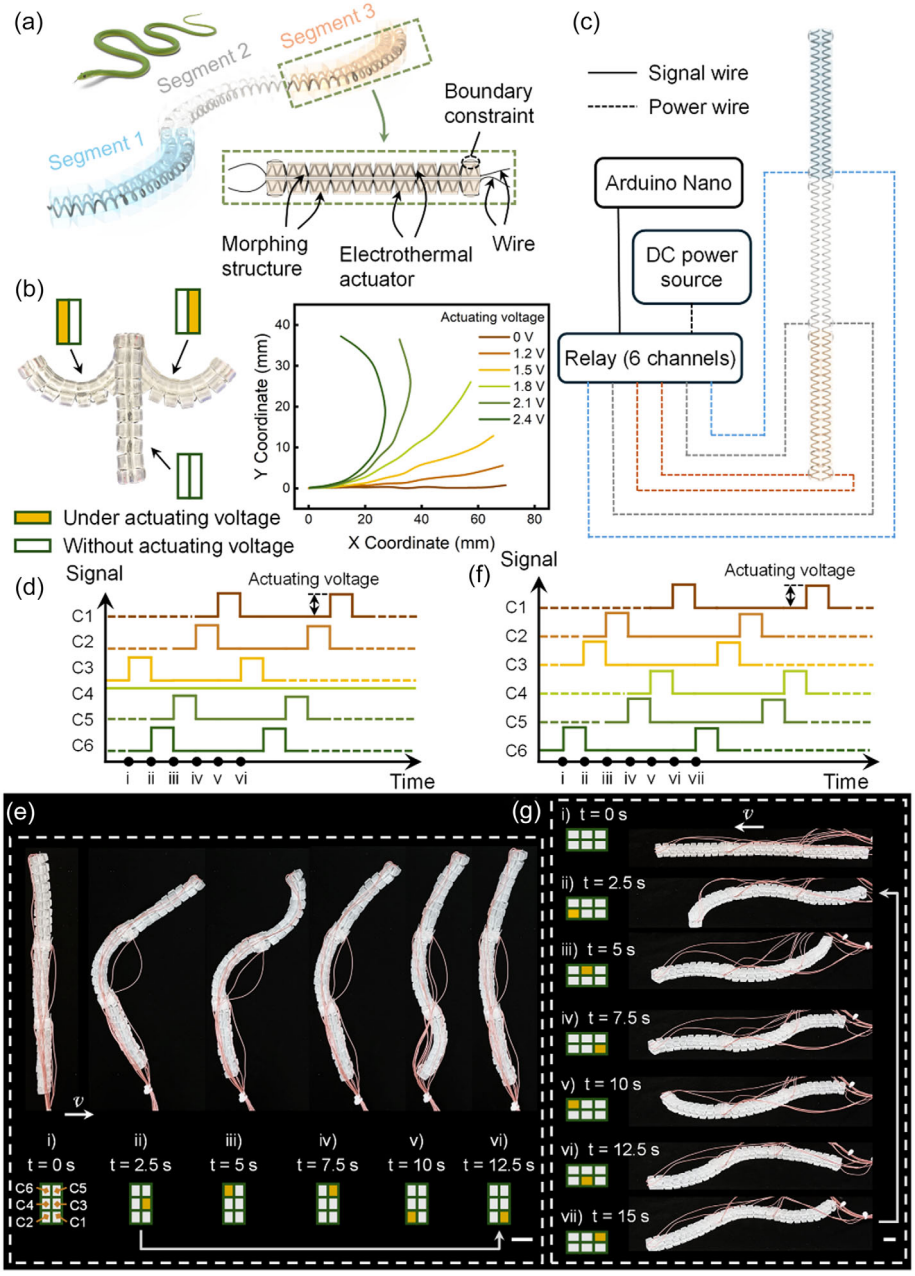


Figure 5. The snake-inspired robot, developed from three double-layer TSAMS segments, demonstrates two locomotion modes. a) Bioinspired design of the snake robot, consisting of three segments, each constructed from two attached TSAMS layers. b) Characterization of bidirectional bending for a single segment of the robot under various actuating voltages. c) The robot's control system, including an Arduino Uno, six single-channel relays, and a DC power source. d) Control signal sequence for the six TSAMS units of the robot operating in sidewinding mode. e) Sequential morphing postures of the robot during sidewinding mode, showing its launch and one control cycle. f) Control signal sequence for the six TSAMS units of the robot operating in lateral undulation mode. g) Sequential morphing postures of the robot during lateral undulation mode, showing its launch and one control cycle.

© 2025 The Author(s). Advanced Intelligent Systems published by Wiley-VCH GmbH

Subsequently, wires are soldered to the tips of SMA springs for electrothermal actuation, and boundary constraints are established between the SMA springs and end particles using steel fibers and UV-light-cured glue (see Figure 1b and Experimental Section for details). The three segments are fabricated separately and then assembled via connecting joints (Figure S13, Supporting Information). Within each segment, the two layers are connected in parallel and can be actuated independently. When one layer is actuated, it deforms to the target shape with minimal constraint from the unactuated layer, owing to the inherent softness of TSAMS. This property enables bidirectional bending by simply applying actuation voltages to different layers of a segment. Figure 5b demonstrates the bidirectional bending of a single segment and shows the morphing curvature under various actuation voltages over a span of 10 s (see Figure S15, Supporting Information for more details).

The control system of the proposed snake-inspired robot is illustrated in Figure 5c and described in detail in Experimental Section. Each of the six SMA spring layers is connected to a DC power source through an individual single-channel relay, enabling independent control. An Arduino Uno delivers actuation signals to these relays, thereby facilitating two distinct locomotion modes—sidewinding and lateral undulation—through different signal sequences.[44,45] Figure 5d depicts the signal sequence for the six TSAMS units during sidewinding. Specifically, the robot cycles through five relay channels in the order C3-C6-C5-C2-C1, causing successive segment morphing that enables motion perpendicular to the robot's body axis (Figure 5e, Movie S10, Supporting Information). In contrast, during lateral undulation, all six channels are sequentially actuated in the order C6-C3-C2-C5-C4-C1. This coordinated actuation produces a periodic traveling wave that propels the robot forward along its body length,[46] as shown in Figure 5f,g. By combining these two locomotion modes, the snake-inspired robot is capable of navigating around obstacles during environmental exploration (Movie S10, Supporting Information). Moreover, the stiffness tuning capability of TSAMS enables the snake-inspired robot to navigate through constrained environments. As shown in Movie S10, supporting Information, the robot can maneuver between obstacles of varying sizes. It is able to displace smaller obstacles (50 g) and wriggle through gaps between larger obstacles weighing 250, 500, and 1000 g, thereby demonstrating its versatility under diverse environmental conditions.

3. Discussion and Conclusion

In this work, we introduce a bioinspired morphing framework, TSAMS, which adopts segmented architectures reminiscent of those observed in nature. This design allows for versatile and programmable morphing capabilities that smoothly transition between soft and rigid states while conforming to target shapes. By combining 3D-printed architected particles with electrothermal actuators, TSAMS excels in both load-bearing capacity and dynamic shape morphing. A central feature of TSAMS is its reconfigurable geometry, enabling it to form complex structures such as arcs, waves, and hooks, as well as to realize advanced gaits for locomotion and sophisticated maneuvers for manipulation. These properties are exemplified by the thermally driven self-rolling robots, 3-DoF soft manipulators, and snake-inspired robots demonstrated in this study, underscoring the potential of TSAMS-based systems in diverse applications ranging from environmental exploration to cargo transport.

Despite these promising results, we acknowledge there remain several challenges and potential areas for future improvement: i) The current TSAMS units are primarily one-dimensional, consisting of a linear array of particles and SMA springs. Expanding them into two or higher dimensions, such as net-like configurations, could lead to more diverse locomotion modes[41,47] and more advanced manipulation capabilities.[48,49] ii) Present designs typically achieve only one programmed shape, limiting posture changes. Incorporating multi-stable elements[50,51] and self-locking features at particle interfaces could enable multiple stable configurations and a higher mechanical response under different operational requirements. iii) Cyclic heating is required for the electrothermal actuators to maintain shape and stiffness. Although the two-layer design mitigates cooling requirements by actuating the opposite side, residual thermal stress can accumulate,[52] leading to inaccuracies in repeated morphing cycles. Exploring alternative actuation methods, such as magnetic actuation, may enhance precision, energy efficiency, and lifespan. iv) While TSAMS provides controllable stiffness, a fully adaptive system that autonomously responds to environmental changes requires integrating sensors and closed-loop feedback. Achieving this would allow the structure to adjust stiffness in real time, enabling more sophisticated responses during tasks like obstacle negotiation and precise manipulation.[10,53]

In summary, the proposed TSAMS framework, with its shape-morphing capabilities and tunable mechanical properties, offers a promising foundation for soft robotic systems requiring both adaptability and robust load-bearing performance.

4. Experimental Section

Design of the Architected Particles: We implemented the following steps to tessellate the target curves into non-interlocking particles. 1) First, the target shapes were designed in 3D modeling software (Rhinoceros 3D, Robert McNeel & Associates), and the particle height was specified. 2) Next, we applied UV mapping to convert the target surface S into a rectangular pattern T. 3) We then represented the resulting tessellation pattern P_0 using a half-edge data structure, where each pair of half-edges shared by faces P_0^i and P_0^j is denoted as e_j^i on P_0^i and e_i^j on P_0^j. Each half-edge e_j^i was augmented with a normalized vector t_j^i, where $e_j^i \perp t_j^i$, and $\|t_j^i\| = 1$, thereby enabling target shape construction. 4) Finally, the tessellated particles were flattened in the plane via rigid-body movements and rotations. After flattening, holes with a diameter of $D_s = 4.3$ mm were created through the particles along the UV directions for inserting the electrothermal actuators in the modeling software (SolidWorks, Dassault Systèmes S.A.).

Fabrication of the TSAMS Unit: To fabricate the architected particles, we employed a stereolithography (SLA) 3D printer (Form3, Formlabs, USA). This approach offers a high spatial resolution (25 μm) and produces parts with precise geometries and good heat resistance, ensuring consistent particle configurations and minimal deformation under actuator heating. After printing, we inserted shape memory alloy (SMA) springs (outer diameter: 4 mm; wire diameter: 0.6 mm; Baohong Company, China) between the particles for electrothermal actuation. Wires were soldered to the ends of the SMA springs to enable actuation in the application of the soft manipulator and snake-inspired robots. For single-layer TSAMS units (Figure 1 and 2), steel fibers (diameter 0.3 mm, Zhongyu Company,

© 2025 The Author(s). Advanced Intelligent Systems published by Wiley-VCH GmbH

China) were tied to the ends of the SMA springs and affixed to the particle boundaries using UV-light-cured glue. In contrast, for multi-layer TSAMS units (Figure 3–5), steel fibers were tied to the ends of each SMA spring before being bundled together to provide boundary constraints (Figure S1, Supporting Information).

Cantilever Bending Tests of TSAMS: For the cantilever-bending tests, we used a piezoelectric force sensor (Changzhou Arizon Technology Co. Ltd) mounted on a screw-driven stepper motor module to measure the applied forces under displacement-controlled loading (Figure S5, Supporting Information). The loading speed was 5 mm s^{-1}, with a maximum displacement of 8 mm. We fixed the TSAMS sample at one end using a 3D-printed clamp attached to the test frame to establish a well-defined cantilever boundary condition. The force sensor was connected to a data acquisition system with a sampling rate of 2000 Hz for continuous force monitoring. To control the actuating voltage, the SMA springs were connected to a DC power source (GPS305D, Shenzhen Guce Electronic Technology Co., Ltd).

Calculation of the Apparent Bending Modulus: We calculated the apparent bending modulus of TSAMS using the following equation[54]

$$E^* = \frac{4KL^3}{bh^3} \tag{1}$$

where K is the slope of the initial linear part of the force–displacement curve (Figure 2e, Figure S5, Supporting Information) and L is the distance from the clamped end to the point of load application at the free end during cantilever-bending tests. b and h are the width and thickness of TSAMS sample, respectively. We used the slope of the initial elastic regime (displacement within ≈0–1 mm) to calculate the bending stiffness K. For the sample tested, $L = 85$ mm, $b = 10$ mm, $h = 10$ mm.

Electro-Thermo-Mechanical Characterization of SMA: We conducted tensile testing, contracting force measurements, and cyclic three-point bending tests using a universal testing machine (Mark-10 Corporation, USA) equipped with a 25 N force sensor. For the tensile tests, we used SMA springs with an initial length of 8 mm and applied loading at a speed of 5 mm s^{-1}, up to a maximum displacement of 40 mm. In the contracting force measurements, we first stretched the SMA springs to 50 mm and fixed them in place. Actuation voltages were applied for ≈10 s, followed by passive cooling under room temperature conditions. For the cyclic bending tests, we assembled a beam-shaped TSAMS sample using nine cubic SLA-printed particles, each with a side length of 10 mm. We performed the test at a loading speed of 12 mm s^{-1}, with a maximum displacement of 15 mm and a three-point bending span of 3 inches (≈76.2 mm). An actuating voltage of 1.6 V was applied at the onset of each loading cycle (i.e., at the highest point), and turned off at the lowest point corresponding to the maximum displacement. We recorded temperature changes during SMA actuation using an infrared thermal imager (K20, HIKMICRO, China).

Design of the Self-Rolling Robot: We selected a 180° arc as the target shape and tessellated it into 10 identical particles, each with a central angle $\varphi = 18°$ (inclined angle $\alpha = 81°$) and a length $l_0 = 7$ mm (Figure S14, Supporting Information). Each particle's cross-section was quadrant-shaped, and assembling four such particles circularly formed a complete circle with an outer diameter $D = 12$ mm. Four holes, each with a diameter of $d = 4.3$ mm, were constructed in a circular array, with a circle diameter of $d_f = \frac{5}{2}\sqrt{2}$ mm for SMA insertion. The particles were then 3D-printed using SLA printer (Form3, Formlabs, USA), and integrated with SMA springs.

Design of the Soft Manipulator: For the twisting base, we began by specifying a twist angle of $\theta = 45°$ and a rotation radius of $R = 25$ mm (Figure 4b). The resulting displacement was then calculated using the following equation

$$d = \frac{R\sin\theta}{\cos\left(\frac{\theta}{2}\right)} \tag{2}$$

To achieve simpler and more precise morphing, we adopted a centrosymmetric design for each TSAMS unit, with $d_f = \frac{1}{2}d$. In this setup, a radius angle of $\beta = 60°$ and a segment length of $l = 10$ mm were selected to ensure smooth and stable deformation. The radius r was subsequently determined by

$$r = \frac{d_f}{1 - \cos\beta} \tag{3}$$

Finally, the top and bottom plates supporting the TSAMS units were designed as squares with a side length of $L = 60$ mm, and the cross sections of the particles were designed as rectangles with a width of $b = 10$ mm and a thickness of $h = 5.5$ mm.

For the end effector, we employed a design analogous to that of the thermally driven self-rolling robot. A 180-degree arc was tessellated into 10 identical particles, each with a quadrant cross-section and an intersection angle of $\gamma = 18°$ between adjacent particles. Four such quadrant units were then assembled in the modeling software to form a complete circle, into which four SMA springs were inserted and wired for actuation. This configuration enables the end effector to bend in four distinct directions by selectively actuating each SMA spring.

Load-Bearing Tests of the Manipulator: We fixed one end of the end effector to the test frame and actuated a single SMA spring at 3 V (GPS305D, Shenzhen Guce Electronic Technology Co., Ltd). After a 5 s actuation period, the end effector reached its target shape, at which point we applied the load (50, 100, and 250 g). Between each test, the end effector was allowed to rest for 3 min to fully cool down and return to its original, unmorphed state before commencing the subsequent test. The curves in Figure 4d were extracted from snapshots of the testing video (Figure S9, Supporting Information).

Controlled Morphing Tests of the Manipulator: We achieved controlled morphing of the end effector by adjusting the actuating voltages in each SMA spring, as demonstrated in Movie S7, Supporting Information. Initially, single-directional bending was realized by actuating one SMA spring at 2.4 V. Once the end effector assumed the target shape, the voltage in this spring was lowered to 1.6 V to maintain the posture, while the adjacent SMA spring was actuated at 2.4 V. Consequently, the end effector morphed in a second direction along a circular path.

Control System of the Snake-Inspired Robot: We used an Arduino Nano to control six single-channel relays (Shenzhen KEYES DIY ROBOT co., Ltd.), which were connected to six TSAMS units, as shown in Figure 5c. The relays were powered by the Arduino Nano through 5 V and GND portals. A DC power source (GPS305D, Shenzhen Guce Electronic Technology Co., Ltd) was connected to the robot through relays to provide an actuating voltage of 4 V.

Curvature-Based Quantitative Analysis of Shape Morphing: To quantitatively evaluate the morphing performance, we calculated the curvature of the deformed structures by fitting a circle to the set of discrete data points representing the centerline of each configuration. Using a least-squares optimization approach, the best-fitting circle was determined, and the curvature was obtained as the reciprocal of the fitted radius. This method was applied to both the end effector under various loads and the segments of the snake-inspired robot under different actuation voltages (Figure S9 and S10, Supporting Information).

Dynamic Loading Test of the Soft Manipulator: To evaluate the manipulator's performance under dynamic loading conditions, we conducted a drop test using a universal testing machine (Mark-10 Corporation, USA) equipped with a 25 N force sensor. The end of the soft manipulator was fixed to the load cell, and a 50 g weight was lifted ≈5 cm above the manipulator before being released to freely fall and hang from its tip (≈0.99 m s^{-1} impact velocity). During the test, the manipulator was actuated at 2.0 V. The force response was recorded at a sampling rate of 500 Hz to capture the transient dynamics.

Supporting Information

Supporting Information is available from the Wiley Online Library or from the author.

© 2025 The Author(s). Advanced Intelligent Systems published by Wiley-VCH GmbH

Acknowledgements

This research was supported by Singapore MOE Tier-2 Award MOE-T2EP50123-0015, and the NAP award (020482) from Nanyang Technological University.

Conflict of Interest

The authors declare no conflict of interest.

Author Contributions

Yu Chen: conceptualization (lead); data curation (lead); formal analysis (lead); investigation (lead); methodology (lead); software (lead); validation (lead); visualization (lead); writing—original draft (lead); writing—review and editing (lead). **Xudong Yang**: data curation (supporting); formal analysis (supporting); investigation (supporting); methodology (supporting); software (supporting); writing—original draft (supporting); writing—review and editing (supporting). **Tianyu Chen**: formal analysis (supporting); investigation (supporting); software (supporting); visualization (supporting); writing—original draft (supporting); writing—review and editing (supporting). **Junwei Li**: formal analysis (supporting); investigation (supporting); software (supporting); writing—original draft (supporting); writing—review and editing (supporting). **Yifan Wang**: conceptualization (lead); funding acquisition (lead); investigation (lead); methodology (lead); project administration (lead); resources (lead); supervision (lead); writing—original draft (supporting); writing—review and editing (supporting).

Data Availability Statement

The data that support the findings of this study are available from the corresponding author upon reasonable request.

Keywords

architected materials, shape memory alloys, shape morphing, soft robotics, tunable stiffness

Received: January 28, 2025
Revised: April 21, 2025
Published online: May 28, 2025

[1] E. Coen, D. J. Cosgrove, *Science* **2023**, *379*, eade8055.
[2] J. W. Truman, L. M. Riddiford, *Nature* **1999**, *401*, 447.
[3] M. Koehl, *Annu. Rev. Ecol. Syst.* **1996**, *27*, 501.
[4] S. Li, K. Wang, *Bioinspiration Biomimetics* **2016**, *12*, 011001.
[5] M. Sakamoto, M. Ruta, C. Venditti, *Proc. R. Soc. B* **2019**, *286*, 20181932.
[6] Å. Flock, D. Strelioff, *Nature* **1984**, *310*, 597.
[7] M. M. Muñoz, *Integr. Comp. Biol.* **2019**, *59*, 705.
[8] M. A. McEvoy, N. Correll, *Science* **2015**, *347*, 1261689.
[9] X. Yang, Y. Zhou, H. Zhao, W. Huang, Y. Wang, K. J. Hsia, M. Liu, *Soft Sci.* **2023**, *3*, 38.
[10] R. Baines, F. Fish, J. Bongard, R. Kramer-Bottiglio, *Nat. Rev. Mater.* **2024**, *9*, 822.
[11] Y. Chen, J. Li, X. Yang, Y. Wang, in *2024 IEEE/RSJ Int. Conf. on Intelligent Robots and Systems (IROS)*, IEEE, Piscataway, NJ **2024**.
[12] Y. Wang, L. Li, D. Hofmann, J. E. Andrade, C. Daraio, *Nature* **2021**, *596*, 238.
[13] X. Kuang, S. Wu, Q. Ze, L. Yue, Y. Jin, S. M. Montgomery, F. Yang, H. J. Qi, R. Zhao, *Adv. Mater.* **2021**, *33*, 2102113.
[14] Y. C. Cheng, H. C. Lu, X. Lee, H. Zeng, A. Priimagi, *Adv. Mater.* **2020**, *32*, 1906233.
[15] F. Zhai, Y. Feng, Z. Li, Y. Xie, J. Ge, H. Wang, W. Qiu, W. Feng, *Matter* **2021**, *4*, 3313.
[16] J. Zhang, Y. Guo, W. Hu, R. H. Soon, Z. S. Davidson, M. Sitti, *Adv. Mater.* **2021**, *33*, 2006191.
[17] F. Hannard, M. Mirkhalaf, A. Ameri, F. Barthelat, *Sci. Robot.* **2021**, *6*, eabf9710.
[18] H. Luan, M. Wang, Q. Zhang, Z. You, Z. Jiao, *Adv. Sci.* **2024**, *11*, 2307350.
[19] Z. Wang, N. M. Freris, X. Wei, *Device* **2024**, *3*, 100246.
[20] T. Ranzani, G. Gerboni, M. Cianchetti, A. Menciassi, *Bioinspiration Biomimetics* **2015**, *10*, 035008.
[21] I. De Falco, M. Cianchetti, A. Menciassi, *Bioinspiration Biomimetics* **2017**, *12*, 056008.
[22] C. B. Frank, *J. Musculoskeletal Neuronal Interact.* **2004**, *4*, 199.
[23] K. Silvipriya, K. K. Kumar, A. R. Bhat, B. D. Kumar, A. John, *J. Appl. Pharm. Sci.* **2015**, *5*, 123.
[24] P. Romano, H. Fabritius, D. Raabe, *Acta Biomater.* **2007**, *3*, 301.
[25] X. Yang, Y. Chen, T. Chen, J. Li, Y. Wang, *Adv. Mater.* **2024**, *36*, 2404502.
[26] X. Yang, M. Liu, B. Zhang, Z. Wang, T. Chen, Y. Zhou, Y. Chen, K. J. Hsia, Y. Wang, *Matter* **2024**, *7*, 603.
[27] K. George, M. Esmaeili, J. Wang, N. Taheri-Qazvini, A. Abbaspourrad, M. Sadati, *Proc. Natl. Acad. Sci.* **2023**, *120*, e2220032120.
[28] L. He, N. Herzig, T. Nanayakkara, P. Maiolino, *Soft Robot.* **2022**, *9*, 1062.
[29] L. Wang, Y. Yang, Y. Chen, C. Majidi, F. Iida, E. Askounis, Q. Pei, *Mater. Today* **2018**, *21*, 563.
[30] X. Yang, Z. Wang, B. Zhang, T. Chen, C. Linghu, K. Wu, G. Wang, H. Wang, Y. Wang, *Adv. Intell. Syst.* **2023**, *5*, 2200250.
[31] X. Yang, M. Liu, T. Chen, Y. Chen, Y. Wang, *Extreme Mech. Lett.* **2024**, *67*, 102121.
[32] Y. Zhao, Y. Chi, Y. Hong, Y. Li, S. Yang, J. Yin, *Proc. Natl. Acad. Sci.* **2022**, *119*, e2200265119.
[33] X. Liang, Y. Ding, Z. Yuan, J. Jiang, Z. Xie, P. Fei, Y. Sun, G. Gu, Z. Zhong, F. Chen, G. Si, Z. Gong, *Mechanics of soft-body rolling motion without external torque*. arXiv preprint arXiv:2410.07644, **2024**.
[34] M. S. Kim, J. K. Heo, H. Rodrigue, H. T. Lee, S. Pané, M. W. Han, S. H. Ahn, *Adv. Mater.* **2023**, *35*, 2208517.
[35] D. Ge, Y. Dai, H. Liang, K. Li, *Int. J. Mech. Sci.* **2024**, *263*, 108780.
[36] Y.-J. Kim, S. Cheng, S. Kim, K. Iagnemma, *IEEE Trans. Robot.* **2013**, *29*, 1031.
[37] W. Dou, W. Dou, G. Zhong, J. Cao, Z. Shi, B. Peng, L. Jiang, *Adv. Mater. Technol.* **2021**, *6*, 2100018.
[38] W. Zhao, J. Wang, Y. Fei, *IEEE/ASME Trans. Mech.* **2021**, *27*, 3751.
[39] X. Qi, H. Shi, T. Pinto, X. Tan, *IEEE Robot. Autom. Lett.* **2020**, *5*, 1610.
[40] J. Ha, *IEEE Trans. Robot.* **2023**.
[41] A. Rafsanjani, Y. Zhang, B. Liu, S. M. Rubinstein, K. Bertoldi, *Sci. Robot.* **2018**, *3*, eaar7555.
[42] T. Takemori, M. Tanaka, F. Matsuno, *IEEE Trans. Robot.* **2018**, *34*, 1384.
[43] R. Ariizumi, F. Matsuno, *IEEE Transactions on Robotics* **2017**, *33*, 1075.
[44] C. Gong, M. J. Travers, H. C. Astley, L. Li, J. R. Mendelson, D. I. Goldman, H. Choset, *Int. J. Robot. Res.* **2016**, *35*, 100.
[45] L. Chen, S. Ma, Y. Wang, B. Li, D. Duan, *Mech. Mach. Theory* **2007**, *42*, 1632.
[46] Y. Cao, Y. Liu, Y. Chen, L. Zhu, Y. Yan, X. Chen, *J. Mech. Phys. Solids* **2017**, *99*, 304.

© 2025 The Author(s). Advanced Intelligent Systems published by Wiley-VCH GmbH

[47] J. W. Booth, D. Shah, J. C. Case, E. L. White, M. C. Yuen, O. Cyr-Choiniere R. Kramer-Bottiglio, *Sci. Robot.* **2018**, *3*, eaat1853.
[48] K. Liu, F. Hacker, C. Daraio, *Sci. Robot.* **2021**, *6*, eabf5116.
[49] E. Brown, N. Rodenberg, J. Amend, A. Mozeika, E. Steltz, M. R. Zakin, H. Lipson, H. M. Jaeger, *Proc. Natl. Acad. Sci.* **2010**, *107*, 18809.
[50] D. Melancon, B. Gorissen, C. J. García-Mora, C. Hoberman, K. Bertoldi, *Nature* **2021**, *592*, 545.
[51] Y. Yang, M. A. Dias, D. P. Holmes, *Phys. Rev. Mater.* **2018**, *2*, 110601.
[52] J. Berman, S. White, *Smart Mater. Struct.* **1996**, *5*, 731.
[53] R. Baines, S. K. Patiballa, J. Booth, L. Ramirez, T. Sipple, A. Garcia, F. Fish, R. Kramer-Bottiglio, *Nature* **2022**, *610*, 283.
[54] F. P. Beer, E. R. Johnston, J. T. DeWolf, D. F. Mazurek, *Mechanics of Materials*, Vol. *1*, mcgraw-Hill New York.

© 2025 The Author(s). Advanced Intelligent Systems published by Wiley-VCH GmbH